

Worst-case amplification of disturbances in inertialess flows of viscoelastic fluids

Binh K. Lieu* Mihailo R. Jovanović* Satish Kumar**

* *Department of Electrical and Computer Engineering, University of Minnesota, Minneapolis, MN 55455 USA (e-mails: lieu006@umn.edu, mihailo@umn.edu)*

** *Department of Chemical Engineering and Material Science, University of Minnesota, Minneapolis, MN 55455 USA (e-mail: kumar030@umn.edu)*

Abstract: Amplification of deterministic disturbances in inertialess channel flows of viscoelastic fluids is studied by analyzing the frequency responses from spatio-temporal body forces to the velocity fluctuations. In strongly elastic flows, we show that velocity fluctuations can exhibit significant amplification even in the absence of inertia. Our analysis demonstrates that streamwise-constant disturbances are the most amplified. Explicit expressions are established for the worst-case amplification of velocity fluctuations arising from different components of the body forces. These show that amplification from the wall-normal and spanwise forces to the streamwise velocity component scales quadratically with the Weissenberg number. The underlying physical mechanism involves stretching of polymer stress fluctuations by a background shear, which is a close analog of the vortex tilting mechanism that is responsible for amplification in inertial flows of Newtonian fluids.

Keywords: Infinite dimensional systems; robustness analysis; elastic turbulence; frequency responses; inertialess flows; polymer stretching; worst-case amplification; viscoelastic fluids.

1. INTRODUCTION

Newtonian fluids, such as air and water, transition to turbulence under the influence of inertia. On the other hand, recent experiments have shown that fluids containing long polymer chains may become turbulent even in low inertial regimes [Larson, 2000, Groisman and Steinberg, 2000, 2004]. Since viscoelastic fluids are often encountered in industrial and biological flows, transition to turbulence in such fluids is important from both fundamental and technological standpoints [Larson, 1992]. Understanding of transition mechanisms in viscoelastic fluids is relevant for polymer processing operations [Larson, 1992] and micro/nano-fluidic device development [Groisman et al., 2003, Groisman and Quake, 2004]. In the former case, turbulence is generally undesirable, except for mixing steps. In the latter case, the addition of polymers has been shown to produce a transition to turbulence, thereby leading to mixing enhancement [Groisman and Steinberg, 2001].

In prior work with a channel flow geometry, we have considered amplification of velocity fluctuations that arises from stochastic spatio-temporal body forces [Hoda et al., 2008, 2009]. However, since the problem of determining variance amplification becomes ill-posed when inertia is completely absent, these results are restricted to cases where the flow has finite inertia. This leaves open the

question of amplification mechanism in inertialess flows of viscoelastic fluids. In the present work, we address this issue by considering worst-case amplification of deterministic disturbances in inertialess channel flows of viscoelastic fluids.

2. PROBLEM FORMULATION

2.1 Governing equations

The momentum, continuity, and constitutive equations for an incompressible channel flow of viscoelastic fluids, with geometry shown in Fig. 1, are given by

$$Re\dot{\mathbf{V}} = We((1 - \beta)\nabla \cdot \mathbf{T} + \beta\nabla^2 \mathbf{V} - \nabla P - Re\mathbf{V} \cdot \nabla \mathbf{V}), \quad (1a)$$

$$0 = \nabla \cdot \mathbf{V}, \quad (1b)$$

$$\dot{\mathbf{T}} = We(\mathbf{T} \cdot \nabla \mathbf{V} + (\mathbf{T} \cdot \nabla \mathbf{V})^T - \mathbf{V} \cdot \nabla \mathbf{T}) \\ \nabla \mathbf{V} + (\nabla \mathbf{V})^T - \mathbf{T}. \quad (1c)$$

Here, dot denotes partial derivative with respect to time t , \mathbf{V} is the velocity vector, P is pressure, \mathbf{T} is the polymer stress tensor, ∇ is the gradient, and ∇^2 is the Laplacian. System (1) has been non-dimensionalized by scaling length with L , velocity with U_0 , polymer stresses with $\eta_p U_0/L$, pressure with $(\eta_s + \eta_p)U_0/L$, and time with λ . Here, U_0 is the largest base flow velocity, L is the channel half-height, and ρ is the fluid density. The key parameters in (1) are: the viscosity ratio, $\beta = \eta_s/(\eta_s + \eta_p)$, where η_s and η_p are the solvent and polymer viscosity, respectively; the

* This work was supported in part by the National Science Foundation under CAREER Award CMMI-06-44793 (to M. R. J.), by the Department of Energy under Award DE-FG02-07ER46415 (to S. K.), and by the University of Minnesota Digital Technology Center's 2010 Digital Technology Initiative Seed Grant (to M. R. J. and S. K.).

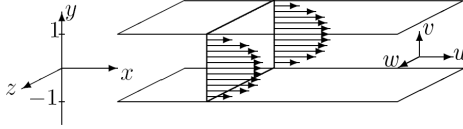


Fig. 1. Geometry of a three-dimensional channel flow.

Weissenberg number, $We = \lambda U_0/L$, which is the ratio of the fluid relaxation time λ to the characteristic flow time L/U_0 ; and the Reynolds number, $Re = \rho U_0 L/(\eta_s + \eta_p)$, which represents the ratio of inertial to viscous forces.

The constitutive equation (1c) is given for an Oldroyd-B fluid. This equation describes the dynamics of polymer stresses and is obtained from a theory of dilute polymer solutions in which each polymer molecule is modeled by two spherical beads connected by a linear spring [Larson, 1999].

Equations (1) exhibit a steady-state solution for the velocities and polymer stresses of the following form

$$\bar{\mathbf{v}} = [U(y) \ 0 \ 0]^T, \\ \bar{\boldsymbol{\tau}} = \begin{bmatrix} \bar{\tau}_{xx} & \bar{\tau}_{xy} & \bar{\tau}_{xz} \\ \bar{\tau}_{xy} & \bar{\tau}_{yy} & \bar{\tau}_{yz} \\ \bar{\tau}_{xz} & \bar{\tau}_{yz} & \bar{\tau}_{zz} \end{bmatrix} = \begin{bmatrix} 2We (U'(y))^2 & U'(y) & 0 \\ U'(y) & 0 & 0 \\ 0 & 0 & 0 \end{bmatrix},$$

where $U(y) = y$ in shear-driven (Couette) flow, $U(y) = 1 - y^2$ in pressure-driven (Poiseuille) flow, and $U'(y) = dU(y)/dy$.

In the absence of inertia, i.e. in flows with $Re = 0$, the equations governing the dynamics (up to the first order) of velocity, $\mathbf{v} = [u \ v \ w]^T$, pressure, p , and polymer stress tensor, $\boldsymbol{\tau}$, fluctuations around the base flow ($\bar{\mathbf{v}}, \bar{\boldsymbol{\tau}}$) are given by

$$0 = -\nabla p + (1 - \beta) \nabla \cdot \boldsymbol{\tau} + \beta \nabla^2 \mathbf{v} + \mathbf{d}, \quad (2a)$$

$$0 = \nabla \cdot \mathbf{v}, \quad (2b)$$

$$\dot{\boldsymbol{\tau}} = \nabla \mathbf{v} + (\nabla \mathbf{v})^T - \boldsymbol{\tau} + We (\boldsymbol{\tau} \cdot \nabla \bar{\mathbf{v}} + \bar{\boldsymbol{\tau}} \cdot \nabla \mathbf{v} + (\bar{\boldsymbol{\tau}} \cdot \nabla \mathbf{v})^T + (\boldsymbol{\tau} \cdot \nabla \bar{\mathbf{v}})^T - \mathbf{v} \cdot \nabla \bar{\boldsymbol{\tau}} - \bar{\mathbf{v}} \cdot \nabla \boldsymbol{\tau}). \quad (2c)$$

Here u , v , and w are the velocity fluctuations in the streamwise (x), wall-normal (y), and spanwise (z) directions, respectively. The momentum equation (2a) is driven by a spatially distributed and temporally varying body forcing, $\mathbf{d} = [d_1 \ d_2 \ d_3]^T$, which we consider to be purely harmonic in the horizontal directions and time, and deterministic in the wall-normal direction.

2.2 State-space representation

We note that (2a) and (2b) can be simplified by expressing the velocity fields in terms of the wall-normal velocity (v) and vorticity ($\eta = \partial_z u - \partial_y w$) fluctuations. This is done by first taking the divergence of (2a) and using (2b) to get an expression for p . This can be used to eliminate p from (2a), yielding an equation for v . The equation for η can be obtained by taking the curl of (2a). Finally, by rearranging the polymer stresses into the state vector $\boldsymbol{\psi} = [\boldsymbol{\psi}_1^T \ \boldsymbol{\psi}_2^T \ \boldsymbol{\psi}_3^T]^T$ with $\boldsymbol{\psi}_1 = [\tau_{yy} \ \tau_{yz} \ \tau_{zz}]^T$, $\boldsymbol{\psi}_2 = [\tau_{xy} \ \tau_{xz}]^T$, and $\boldsymbol{\psi}_3 = \tau_{xx}$, we arrive at the following static-in-time expression for v and η in terms of the polymer stress and body forcing fluctuations

$$\begin{aligned} v &= \mathbf{C}_v \boldsymbol{\psi} + \mathbf{D}_v \mathbf{d}, \\ \eta &= \mathbf{C}_\eta \boldsymbol{\psi} + \mathbf{D}_\eta \mathbf{d}. \end{aligned} \quad (3)$$

In addition, equation (2c) can be brought to the following form

$$\begin{aligned} \dot{\boldsymbol{\psi}}_1 &= \mathbf{F}_{11} \boldsymbol{\psi}_1 + \mathbf{F}_{1v} v + \mathbf{F}_{1\eta} \eta, \\ \dot{\boldsymbol{\psi}}_2 &= \mathbf{F}_{21} \boldsymbol{\psi}_1 + \mathbf{F}_{22} \boldsymbol{\psi}_2 + \mathbf{F}_{2v} v + \mathbf{F}_{2\eta} \eta, \\ \dot{\boldsymbol{\psi}}_3 &= \mathbf{F}_{32} \boldsymbol{\psi}_2 + \mathbf{F}_{33} \boldsymbol{\psi}_3 + \mathbf{F}_{3v} v + \mathbf{F}_{3\eta} \eta. \end{aligned} \quad (4)$$

Finally, substitution of (3) into (4) along with the applications of the Fourier transform in x and z yields the state-space representation of system (2)

$$\begin{aligned} \dot{\boldsymbol{\psi}}(\boldsymbol{\kappa}, y, t) &= \mathbf{A}(\boldsymbol{\kappa}) \boldsymbol{\psi}(\boldsymbol{\kappa}, y, t) + \mathbf{B}(\boldsymbol{\kappa}) \mathbf{d}(\boldsymbol{\kappa}, y, t), \\ \mathbf{v}(\boldsymbol{\kappa}, y, t) &= \mathbf{C}(\boldsymbol{\kappa}) \boldsymbol{\psi}(\boldsymbol{\kappa}, y, t) + \mathbf{D}(\boldsymbol{\kappa}) \mathbf{d}(\boldsymbol{\kappa}, y, t), \end{aligned} \quad (5)$$

where $\boldsymbol{\kappa} = [k_x \ k_z]^T$ with k_x and k_z representing the horizontal wavenumbers. The output in (5) is determined by the velocity fluctuations. Due to space limitation, the underlying operators will be reported elsewhere.

The boundary conditions on the wall-normal velocity and vorticity are dictated by the no-slip and no-penetration requirements

$$v(\boldsymbol{\kappa}, y = \pm 1, t) = v'(\boldsymbol{\kappa}, y = \pm 1, t) = \eta(\boldsymbol{\kappa}, y = \pm 1, t) = 0.$$

We note that there are no boundary conditions on the polymer stresses.

2.3 Spatio-temporal frequency responses

The frequency response of system (5) is given by

$$\mathbf{H}(\boldsymbol{\kappa}, \omega; We, \beta) = \mathbf{C}(\boldsymbol{\kappa}) (i\omega \mathbf{I} - \mathbf{A}(\boldsymbol{\kappa}))^{-1} \mathbf{B}(\boldsymbol{\kappa}), \quad (6)$$

For a stable generator \mathbf{A} , (6) describes the steady-state response to harmonic input signals across spatial wavenumbers (k_x, k_z) and temporal frequency ω . Namely, if the input is harmonic in x , z , and t , i.e., $\mathbf{d}(y, z, t) = \bar{\mathbf{d}}(y) e^{i(\bar{k}_x x + \bar{k}_z z + \bar{\omega} t)}$, with $\bar{\mathbf{d}}(y)$ denoting some spatial distribution in the wall-normal direction, then the output is also harmonic in x , z , and t with the same frequencies but with a modified amplitude and phase

$$\begin{aligned} \mathbf{v}(x, y, z, t) &= ([\mathbf{H}(\bar{k}_x, \bar{k}_z, \bar{\omega}) \bar{\mathbf{d}}](y)) e^{i(\bar{k}_x x + \bar{k}_z z + \bar{\omega} t)} \\ &= \left(\int_{-1}^1 \mathbf{H}_k(\bar{k}_x, \bar{k}_z, \bar{\omega}; y, \xi) \mathbf{d}(\xi) d\xi \right) e^{i(\bar{k}_x x + \bar{k}_z z + \bar{\omega} t)}, \end{aligned}$$

where the amplitude and phase are precisely determined by the frequency response at the input frequencies $(\bar{k}_x, \bar{k}_z, \bar{\omega})$. Here \mathbf{H}_k denotes the kernel representation of the frequency response operator. Note that we have dropped the dependence of the frequency response operator on We and β for notational convenience.

The n th singular value of the frequency response operator \mathbf{H} is determined by

$$\sigma_n^2(\mathbf{H}) = \lambda_n(\mathbf{H}^* \mathbf{H}),$$

where $\lambda_n(\cdot)$ denotes the n th eigenvalue of a given operator. For any (k_x, k_z, ω) , $\sigma_{\max}(\mathbf{H}) = \max_n \sigma_n(\mathbf{H})$ determines the largest amplification from \mathbf{d} to \mathbf{v} . Furthermore, the temporal-supremum of the maximal singular value of \mathbf{H} determines the so-called H_∞ norm of system (5) [Zhou et al., 1996]

$$G(\boldsymbol{\kappa}; We, \beta) = \sup_{\omega} \sigma_{\max}^2(\mathbf{H}(\boldsymbol{\kappa}, \omega; We, \beta)).$$

This measure of input-output amplification has several appealing interpretations:

- (a) for any (k_x, k_z) , the H_{∞} norm represents the worst case amplification of purely harmonic (in x , z , and t) deterministic (in y) disturbances. This worst-case input-output gain is obtained by maximizing over input temporal frequencies (sup over ω) and wall-normal shapes (maximal singular value of \mathbf{H});
- (b) in the temporal domain, the H_{∞} norm represents the energy gain for the forcing with the worst possible frequency distribution

$$G(\boldsymbol{\kappa}) = \sup_{E_d(\boldsymbol{\kappa}) \leq 1} \frac{E_v(\boldsymbol{\kappa})}{E_d(\boldsymbol{\kappa})},$$

where $E_v(\boldsymbol{\kappa})$ denotes the $\boldsymbol{\kappa}$ -parameterized energy of velocity fluctuations, i.e.,

$$E_v(\boldsymbol{\kappa}) = \int_0^{\infty} \int_{-1}^1 \mathbf{v}^*(\boldsymbol{\kappa}, y, t) \mathbf{v}(\boldsymbol{\kappa}, y, t) dy dt.$$

In other words, for a unit-energy forcing, G captures the largest possible energy of velocity fluctuations;

- (c) at any (k_x, k_z) , the inverse of the H_{∞} norm quantifies the size of an additive unstructured modeling uncertainty $\boldsymbol{\Gamma}$ that can destabilize generator \mathbf{A} in (5). Namely, large H_{∞} norms indicate small stability margins (i.e., bad robustness properties to modeling imperfections). For systems with bad robustness properties, even small modeling uncertainties (captured by operator $\boldsymbol{\Gamma}$) can lead to instability of operator $\mathbf{A} + \boldsymbol{\Gamma}$.

We finally note that the frequency response of system (5) can be further decomposed into 3×3 block-operator form

$$\begin{bmatrix} u \\ v \\ w \end{bmatrix} = \begin{bmatrix} \mathbf{H}_{u1} & \mathbf{H}_{u2} & \mathbf{H}_{u3} \\ \mathbf{H}_{v1} & \mathbf{H}_{v2} & \mathbf{H}_{v3} \\ \mathbf{H}_{w1} & \mathbf{H}_{w2} & \mathbf{H}_{w3} \end{bmatrix} \begin{bmatrix} d_1 \\ d_2 \\ d_3 \end{bmatrix}. \quad (7)$$

The above form is suitable for identifying the forcing components that introduce the largest amplification of the velocity fluctuations. In (7), \mathbf{H}_{rj} maps d_j to r , and $G_{rj}(\boldsymbol{\kappa}; We, \beta) = \sup_{\omega} \sigma_{\max}^2(\mathbf{H}_{rj}(\boldsymbol{\kappa}, \omega; We, \beta))$ with $r = \{u, v, w\}$ and $j = \{1, 2, 3\}$. The finite-dimensional approximations of the underlying operators are obtained using the pseudospectral method [Weideman and Reddy, 2000]. After discretization in the wall-normal direction, each component in (7) becomes an $N \times N$ matrix, where N denotes the number of Chebyshev collocation points in y . All computations are performed in MATLAB, and a fast algorithm [Bruinsma and Steinbuch, 1990] is implemented to compute the H_{∞} norm. Finally, additional computations with larger number of grid points in y were used to confirm convergence of our results.

3. FREQUENCY RESPONSES OF 3D VELOCITY FLUCTUATIONS

In this section, we consider three dimensional fluctuations in inertialess Poiseuille flow. We compute the worst-case amplification of velocity fluctuations and identify the corresponding wavenumbers that are most amplified. Our analysis shows that velocity fluctuations with large streamwise and $\mathcal{O}(1)$ spanwise length scales are most sensitive

to disturbances. We further utilize the component-wise frequency responses to identify forcing components that have the strongest influence on the velocity fluctuations. We illustrate that the wall-normal and spanwise forces have the highest impact, and that the streamwise velocity is most amplified by the system's dynamics.

We first analyze the effect of viscosity ratio β and Weissenberg number We on the amplification of velocity fluctuations. In flows with $We = 50$ and $\beta = \{0.1, 0.5, 0.9\}$, Fig. 2 shows the worst-case amplification of velocity fluctuations in the presence of all three body forces. For $\beta = 0.1$, the peak amplification takes place at $(k_x = k_z = 0)$; see Fig. 2(a). We observe that the amplification of velocity fluctuations decreases with increasing β . In addition, for $\beta = 0.5$, a new peak starts to emerge in a narrow region near $k_x \approx 0$ and $k_z \approx 2$ and, for $\beta = 0.9$, the small wavenumbers again become dominant. In Section 4, we explain these observations by developing explicit scaling relationships of the worst-case amplification for streamwise constant fluctuations.

Figure 3 shows the worst-case amplification of velocity fluctuations triggered by all three body forces in flows with $We = \{10, 50, 100\}$ and $\beta = 0.5$. We see that the velocity fluctuations become more amplified as We increases. For $We = 10$, the peak amplification is located in a region where $k_x \approx 0$ and $k_z \approx 0$ (cf. Fig. 3(a)). However, as We increases to 50, a dominant peak appears at nonzero value of k_z and, as We increases to 100, this peak value gets significantly larger than the amplification at other wavenumbers. In flows with large enough We , the streamwise-elongated and spanwise periodic flow fluctuations are the most amplified by deterministic body forces. This suggest that in strongly elastic channel flows, the streamwise-constant fluctuations are most sensitive to external disturbances.

We next study the frequency responses from different forcing components to different velocity components. This analysis enables us to identify forcing components that are most effective in amplifying velocity fluctuations. Figure 4 shows the worst-case amplification of selected frequency response components in (7) for Poiseuille flow with $We = 50$ and $\beta = 0.5$. The streamwise velocity fluctuations are the most amplified and this high amplification is triggered by d_2 and d_3 . Furthermore, the maximum amplification in these two responses occurs at $k_x \approx 0$ and $k_z \approx \mathcal{O}(1)$. This illustrates that streamwise velocity fluctuations are responsible for the most amplified region ($k_x \approx 0$, $k_z \approx 2$) in Fig 3(b). On the other hand, the yellow region in figure 3(b) arises from the responses of streamwise and spanwise velocity fluctuations to d_1 and d_3 , respectively. Since the amplification of the wall-normal velocity is much smaller than that of the other two velocity components, we have not shown the frequency responses of v in Fig. 4.

The results of this section clearly illustrate the dominance of streamwise-constant and nearly streamwise-constant velocity fluctuations. The streamwise velocity is most amplified by disturbances and this large response is caused by the wall-normal and spanwise body forces. In addition, energy amplification gets larger with increase in the Weissenberg number; this suggests that the increase in polymer

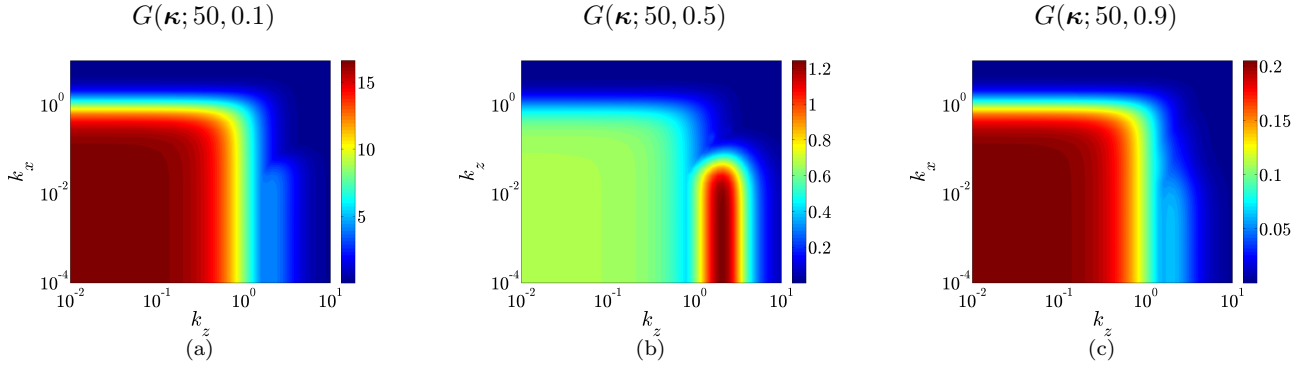


Fig. 2. Worst-case amplification from \mathbf{d} to \mathbf{v} in Poiseuille flow with $We = 50$ and: (a) $\beta = 0.1$; (b) $\beta = 0.5$; and (c) $\beta = 0.9$.

relaxation time enhances amplification in inertialess flows of viscoelastic fluids.

4. DEPENDENCE OF WORST-CASE AMPLIFICATION ON THE WEISSENBERG NUMBER

Motivated by the observation that the most amplified velocity fluctuations have large streamwise length-scale, we next examine the linearized model at $k_x = 0$. We use this model to establish an explicit scaling of the frequency responses with We and β , and explain the observations made in Section 3. In particular, we demonstrate that the worst-case amplification from wall-normal and spanwise forcing to the streamwise velocity scales quadratically with the Weissenberg number. Furthermore, we show that this We -scaling comes from the stretching of polymer stress fluctuations by base shear.

4.1 Streamwise-constant model

In the absence of streamwise variations (i.e., at $k_x = 0$), τ_{xx} does not influence the dynamics of ψ_1 and ψ_2 and as a result, τ_{xx} has no impact on the dynamics of velocity fluctuations. This allows us to rewrite (4) and (3) as

$$\dot{\psi}_1 = -\psi_1 + \mathbf{F}_{1v}v, \quad (8a)$$

$$\dot{\psi}_2 = We(\mathbf{F}_{21}\psi_1 + \mathbf{F}_{2v}v) + (-\psi_2 + \mathbf{F}_{2\eta}\eta), \quad (8b)$$

$$v = \mathbf{C}_{v1}\psi_1 + \mathbf{D}_{v2}d_2 + \mathbf{D}_{v3}d_3, \quad (8c)$$

$$\eta = \mathbf{C}_{\eta2}\psi_2 + \mathbf{D}_{\eta1}d_1. \quad (8d)$$

Now, substitution of (8c) and (8d) into (8a) and (8b) can be used to obtain a state-space representation of a streamwise-constant linearized model. Alternatively, polymer stresses can be eliminated from the model by substituting the temporal Fourier transform of (8a) and (8b) into (8c) and (8d). This implies that \mathbf{H} in (7) can be simplified to

$$\begin{bmatrix} u \\ v \\ w \end{bmatrix} = \begin{bmatrix} \bar{\mathbf{H}}_{u1} & We\bar{\mathbf{H}}_{u2} & We\bar{\mathbf{H}}_{u3} \\ 0 & \bar{\mathbf{H}}_{v2} & \bar{\mathbf{H}}_{v3} \\ 0 & \bar{\mathbf{H}}_{w2} & \bar{\mathbf{H}}_{w3} \end{bmatrix} \begin{bmatrix} d_1 \\ d_2 \\ d_3 \end{bmatrix}, \quad (9)$$

where the We -independent operators $\bar{\mathbf{H}}_{rj}$ are given by

$$\begin{aligned} \bar{\mathbf{H}}_{u1}(k_z, \omega; \beta) &= \frac{i\omega + 1}{i\omega\beta + 1} \mathbf{C}_{u\eta} \mathbf{D}_\eta, \\ \bar{\mathbf{H}}_{u2}(k_z, \omega; \beta) &= \frac{(1 - \beta)}{(i\omega\beta + 1)^2} \mathbf{C}_{u\eta} \mathbf{C}_{\eta2} \mathbf{F}_{21} \mathbf{F}_{1v} \mathbf{D}_{v2}, \\ \bar{\mathbf{H}}_{u3}(k_z, \omega; \beta) &= \frac{(1 - \beta)}{(i\omega\beta + 1)^2} \mathbf{C}_{u\eta} \mathbf{C}_{\eta2} \mathbf{F}_{21} \mathbf{F}_{1v} \mathbf{D}_{v3}, \\ \bar{\mathbf{H}}_{v2}(k_z, \omega; \beta) &= \frac{i\omega + 1}{i\omega\beta + 1} \mathbf{D}_{v2}, \\ \bar{\mathbf{H}}_{v3}(k_z, \omega; \beta) &= \frac{i\omega + 1}{i\omega\beta + 1} \mathbf{D}_{v3}, \\ \bar{\mathbf{H}}_{w2}(k_z, \omega; \beta) &= \frac{i\omega + 1}{i\omega\beta + 1} \mathbf{C}_{wv} \mathbf{D}_{v2}, \\ \bar{\mathbf{H}}_{w3}(k_z, \omega; \beta) &= \frac{i\omega + 1}{i\omega\beta + 1} \mathbf{C}_{wv} \mathbf{D}_{v3}. \end{aligned}$$

These can be used to obtain explicit expressions for the worst-case amplification from different forcing to different velocity components. For example, the worst-case amplification from d_2 to u is given by

$$\begin{aligned} G_{u2}(k_z; We, \beta) &= \sup \sigma_{\max}^2(H_{u2}(k_z, \omega; We, \beta)) \\ &= We^2 \sup \sigma_{\max}^2(\bar{\mathbf{H}}_{u2}(k_z, \omega; \beta)) \\ &= We^2 (1 - \beta)^2 \sigma_{\max}^2(\mathbf{C}_{u\eta} \mathbf{C}_{\eta2} \mathbf{F}_{21} \mathbf{F}_{1v} \mathbf{D}_{v2}) \\ &= We^2 (1 - \beta)^2 g_{u2}(k_z), \end{aligned}$$

where the function g_{u2} captures the spanwise frequency response (from d_2 to u) and is independent of We and β . Using a similar procedure, we can obtain the following expression for the worst-case amplification from d_j to r

$$\begin{bmatrix} G_{u1} & G_{u2} & G_{u3} \\ G_{v1} & G_{v2} & G_{v3} \\ G_{w1} & G_{w2} & G_{w3} \end{bmatrix} = \begin{bmatrix} f_{u1}(k_z)/\beta^2 & We^2(1 - \beta)^2 g_{u2}(k_z) & We^2(1 - \beta)^2 g_{u3}(k_z) \\ 0 & f_{v2}(k_z)/\beta^2 & f_{v3}(k_z)/\beta^2 \\ 0 & f_{w2}(k_z)/\beta^2 & f_{w3}(k_z)/\beta^2 \end{bmatrix}, \quad (10)$$

where the functions f and g represent the We - and β -independent spanwise frequency responses of system (5) at $k_x = 0$.

The base-flow-independent functions $f_{rj}(k_z)$ with $\{r = v, w; j = 1, 2\}$, are shown in Fig. 5. We see that f_{v2} and f_{v3}

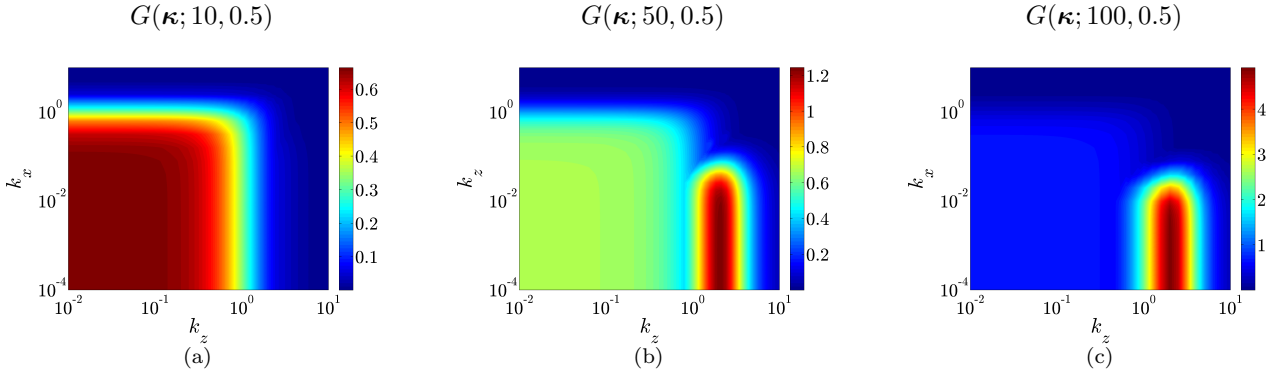


Fig. 3. Worst-case amplification from \mathbf{d} to \mathbf{v} in Poiseuille flow with $\beta = 0.5$ and: (a) $We = 10$; (b) $We = 50$; and (c) $We = 100$.

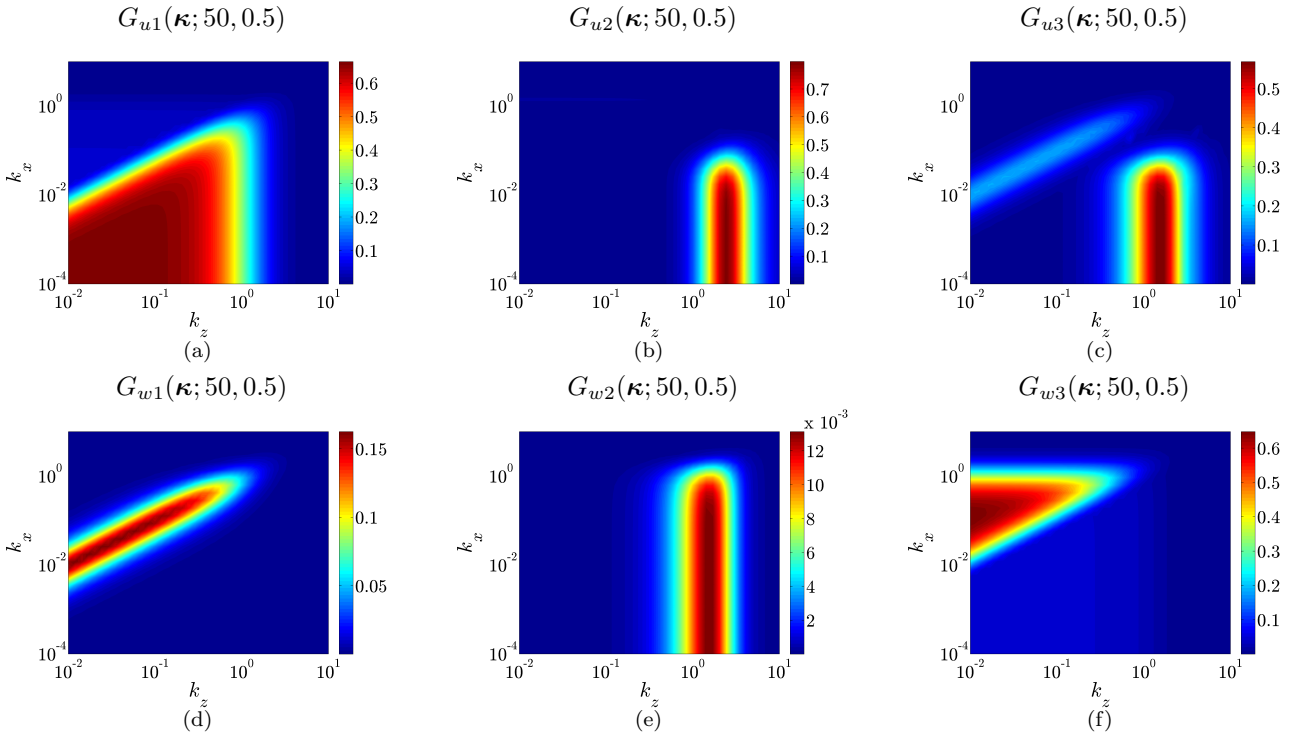


Fig. 4. Worst-case amplification from d_j to r with $r = \{u, w\}$ and $j = \{1, 2, 3\}$ in Poiseuille flow with $We = 50$ and $\beta = 0.5$.

exhibit similar trends with peaks at $\mathcal{O}(1)$ values of k_z . On the other hand, f_{w3} has a low-pass shape with maximum occurring at $k_z = 0$. The peak value of this function is about four times larger than the peak values of f_{v2} and $f_{v3} = f_{w2}$.

The functions characterizing the largest amplification of u caused by d_1 , d_2 , and d_3 are shown in Fig. 6. From Fig. 6(a), we observe that f_{u1} has high values for low spanwise wavenumbers. The k_z -dependence of f_{u1} is similar to that of f_{w3} , but much larger in magnitude (cf. Figs. 6(a) and 5(b)). On the other hand, functions g_{u2} and g_{u3} have peak values at $k_z \approx \mathcal{O}(1)$. For completeness, in Figs. 6(b) we also show the worst-case amplification of u in the presence of $[d_2 \ d_3]^T$, $g_{u,23}$. We note that the peak values of the g -functions are almost two orders of magnitude smaller than the peak value of f_{u1} . However, since G_{u2} and G_{u3} in (10) are proportional to We^2 , as the

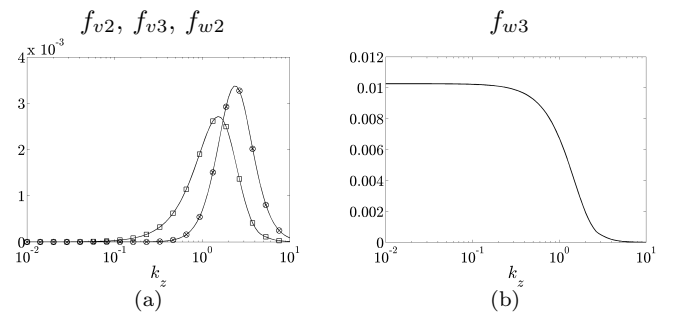


Fig. 5. Functions characterizing worst-case amplification from d_2 and d_3 to v and w ; $f_{rj}(k_z)$ with $\{r = v, w; j = 1, 2\}$. (a) f_{v2} (\square), f_{v3} (\circ), and f_{w2} (\times); and (b) f_{w3} .

Weissenberg number increases d_2 and d_3 are going to have more pronounced influence on u than d_1 .

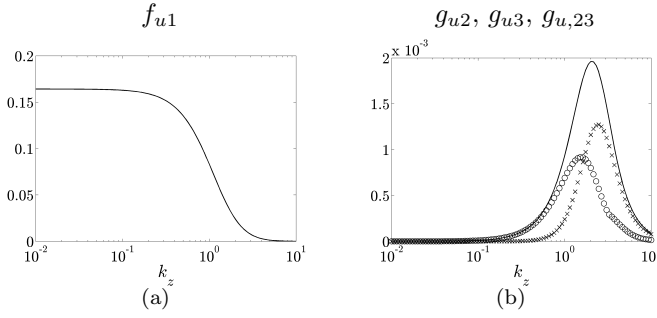


Fig. 6. Functions characterizing the worst-case amplification from d_1 , d_2 , d_3 , and $[d_2 \ d_3]^T$ to u . (a) f_{u1} ; and (b) g_{u2} (\times), g_{u3} (\circ), and $g_{u,23}$ (solid) in Poiseuille flow.

The effect of β on the amplification of velocity fluctuations is captured by (10). Note that G_{u2} and G_{u3} scale as $(1 - \beta)^2$, while the other G -functions in (10) scale as $1/\beta^2$. Thus, in the Newtonian limit (i.e., as β increases to 1) the influence of disturbances on velocity fluctuations is reduced and governed by viscous dissipation.

The results of this section can be used to clarify the observations made in Section 3. Since the streamwise velocity is most amplified by disturbances, we consider the peak value of the spanwise frequency responses from d_j to u

$$\tilde{G}_{uj}(We, \beta) = \sup_{k_z} G_{uj}(k_z; We, \beta).$$

In flows with $We = 50$, we have

- (i) for $\beta = 0.1$, $\tilde{G}_{u1} \approx 16.42$ and $\tilde{G}_{u2} \approx 2.58$;
- (ii) for $\beta = 0.5$, $\tilde{G}_{u1} \approx 0.66$ and $\tilde{G}_{u2} \approx 0.80$; and
- (iii) for $\beta = 0.9$, $\tilde{G}_{u1} \approx 0.2$ and $\tilde{G}_{u2} \approx 0.03$.

Therefore, for $\beta = 0.1$, d_1 triggers the largest response of u , implying dominance of small spanwise wavenumbers (cf. Fig. 2(a)). As β increases to 0.5, influence of d_2 and d_3 becomes more important leading to the peaks at $k_z \approx 2$ (cf. Fig. 2(b)). Finally, for $\beta = 0.9$, f_{u1} again takes over as reflected in the peaks around $k_z = 0$ in Fig. 2(c). Similar argument can be used to explain shifting of the peaks from $k_z \approx 0$ to $k_z \approx 2$ as We gets increased in Fig. 3.

We next discuss the physical mechanisms responsible for large amplification of streamwise velocity fluctuations in flows with high We . The key ingredient responsible for providing We^2 -scaling of G_{u2} and G_{u3} is the operator \mathbf{F}_{21} , which couples ψ_1 to ψ_2 . Without this operator, all responses would be We -independent and dynamics of velocity fluctuations in inertialess channel flows of viscoelastic fluids would be dominated by viscous dissipation. A careful examination of the constitutive equation (2c) shows that, from a physical point of view, \mathbf{F}_{21} accounts the stretching of polymer stress fluctuations by base shear (i.e., $\boldsymbol{\tau} \cdot \nabla \mathbf{v}$). We note that the polymer stretching mechanism has been recently identified as the primary cause behind large transient growth of the velocity and polymer stress fluctuations in Jovanović and Kumar [2010, 2011].

5. CONCLUDING REMARKS

In this study, we have analyzed non-modal amplification of disturbances in inertialess channel flows of viscoelastic

fluids by studying the frequency responses from body forces to the velocity fluctuations. The results presented here illustrate that the velocity fluctuations can experience significant amplification even when inertial effects are negligible. This demonstrates that small modeling uncertainties can destabilize nominally stable flows even in the absence of inertia. This uncertainty may arise from inevitable imperfections in the laboratory environment or from the approximate nature of the governing equations.

Our ongoing efforts are directed towards examining the influence of disturbances on the dynamics of polymer stress fluctuations. This analysis is expected to enhance the understanding of the early stages of transition to elastic turbulence in channel flows of viscoelastic fluids.

REFERENCES

- N. A. Bruinsma and M. Steinbuch. A fast algorithm to compute the H_∞ -norm of a transfer function matrix. *Systems & Control Letters*, 14:287 – 293, 1990.
- A. Groisman and S. R. Quake. A microfluidic rectifier: anisotropic flow resistance at low Reynolds numbers. *Phys. Rev. Lett.*, 92(9):094501, 2004.
- A. Groisman and V. Steinberg. Elastic turbulence in a polymer solution flow. *Nature*, 405:53–55, 2000.
- A. Groisman and V. Steinberg. Efficient mixing at low Reynolds numbers using polymer additives. *Nature*, 410: 905–908, 2001.
- A. Groisman and V. Steinberg. Elastic turbulence in curvilinear flows of polymer solutions. *New J. Phys.*, 6:29, 2004.
- A. Groisman, M. Enzelberger, and S. R. Quake. Microfluidic memory and control devices. *Science*, 300(5621): 955–958, 2003.
- N. Hoda, M. R. Jovanović, and S. Kumar. Energy amplification in channel flows of viscoelastic fluids. *J. Fluid Mech.*, 601:407–424, April 2008.
- N. Hoda, M. R. Jovanović, and S. Kumar. Frequency responses of streamwise-constant perturbations in channel flows of Oldroyd-B fluids. *J. Fluid Mech.*, 625:411–434, April 2009.
- M. R. Jovanović and S. Kumar. Transient growth without inertia. *Phys. Fluids*, 22(2):023101, February 2010.
- M. R. Jovanović and S. Kumar. Nonmodal amplification of stochastic disturbances in strongly elastic channel flows. *J. Non-Newton. Fluid Mech.*, 2011. in press.
- R. G. Larson. Instabilities in viscoelastic flows. *Rheol. Acta*, 31:213–263, 1992.
- R. G. Larson. *The Structure and Rheology of Complex Fluids*. Oxford University Press, 1999.
- R. G. Larson. Turbulence without inertia. *Nature*, 405: 27–28, 2000.
- J. A. Weideman and S. C. Reddy. A MATLAB differentiation matrix suite. *ACM T. Math. Software*, 26:465 – 519, 2000.
- K. Zhou, J. C. Doyle, and K. Glover. *Robust and Optimal Control*. Prentice Hall, New Jersey, 1996.